

Fragile dense suspensions under shear rotation

Frédéric Blanc,¹ François Peters,¹ Jurriaan J.J. Gillissen,² Michael E. Cates,³ Sandra Bosio,¹ Camille Benarroche,¹ and Romain Mari⁴

¹*Université Côte d'Azur, CNRS, Institut de Physique de Nice (INPHYNI), France*

²*The Technology Partnership, Science Park, Melbourn, UK.*

³*DAMTP, Centre for Mathematical Sciences, University of Cambridge, Wilberforce Road, Cambridge CB3 0WA, UK*

⁴*Université Grenoble Alpes & CNRS, LIPhy, 38000 Grenoble, France*

(Dated: December 6, 2022)

While quasi-Newtonian complex fluids under steady-state flow, dense non-Brownian suspensions exhibit complex “macro-fragile” behaviors under unsteady flow conditions, as revealed by abrupt shear inversions (reversals). Here, we introduce an experimental setup to systematically explore their macro-fragile response to shear rotations, where one suddenly rotates the principal axes of shear by an angle θ . This reveals a transient decrease of the shear stress under shear rotation. Moreover, the orthogonal shear stress, which vanishes in steady state, takes non-negligible values with a rich θ -dependence, changing qualitatively with solid volume fraction ϕ , and resulting in a force that tends to reduce or enhance the direction of flow for small or large ϕ . These findings are confirmed and rationalized by particle-based numerical simulations and a recently proposed constitutive model. We show that the rotation angle dependence of the orthogonal stress results from a ϕ -dependent interplay between hydrodynamic and contact stresses.

Suspensions of non-Brownian hard particles in liquid form a large class of complex fluids [1, 2]. When solid and fluid are mixed in roughly equal proportion, they are called dense suspensions. Their widespread use in industry calls for the development of proper constitutive characterization and modelling, in order to enable reliable quantitative process design.

In steady state, the viscosity of non-Brownian suspensions is observed to be either deformation-rate-independent [3, 4] or slightly shear thinning [5–9]. Shear thickening is also observed when particles are repulsive beyond pure hard-core forces [10, 11], but we here focus on the strictly hard-sphere case. The viscosity increases with the solid volume fraction ϕ , and diverges at the jamming volume fraction ϕ_J [3, 4]. However, dense suspensions exhibit striking unsteady behaviors, e.g. the sharp viscosity drop in orthogonal superposition [12–17]. In shear reversal, where a suspension initially sheared in steady state under a given deformation rate $\dot{\gamma}$ is suddenly sheared with a rate $-\dot{\gamma}$, the viscosity drops suddenly at reversal, passes through a minimum value and climbs up to its steady-state value after a few strain units [18–25].

Under shear, suspensions develop an anisotropic contact network which takes up most of the stress at large concentrations [10, 22, 26–31] and is built in a finite strain [18]. Upon shear reversal, the micro-structure is initially not compliant with the new direction of shear, leading to a viscosity dip which ends when the micro-structure is rebuilt in the new orientation [18]. The fact that the principal axes of the micro-structure have to rotate during a finite strain interval to sustain a change of applied load direction is known as macrofragility [32, 33]. For shear reversal, the rotation of the strain axes is maximal, as the compressional and elongational axes are swapped. The associated macro-fragile response has been

carefully characterized numerically [23, 24, 34].

Beyond shear reversal, characterization of the fragility of dense suspensions is however absent. Here we fill this gap by considering the response to *shear rotations*, i.e. rotations of the strain axes by an arbitrary angle θ about the gradient direction. We perform shear rotations in experiments, with a specifically designed rheometer, discrete element simulations, and the Gillissen-Wilson constitutive model [35, 36]. We report the viscosity drop as a function of angle θ and post-rotation strain γ .

We also unveil a new non-Newtonian phenomenon: following a shear rotation, the shear viscosity orthogonal to the flow direction, η_{32} , is transiently finite, reaching up to 50% of the usual shear viscosity η_{12} for large ϕ . Moreover, we show that the nature of angular dependence of η_{32} depends on ϕ : while at moderate ϕ , η_{32} shows a change of sign in $\theta \in [0, \pi]$, associated to a force resisting shear rotation for small θ values, for the largest ϕ values it keeps a constant sign. We show that this is due to the decreasing relative contribution of hydrodynamic stresses versus contact stresses when ϕ increases.

Experimental setup We designed a *cross rheometer* [37], sketched in Fig. 1, made with two parallel plates mounted on two motorized linear stages of 25mm stroke (Newport MFA-CC) acting in perpendicular directions, allowing for arbitrary relative parallel motion and therefore arbitrary simple shear with velocity gradient orthogonal to the plates. We apply a simple shear (Fig. 1(b)) with velocity gradient $\mathbf{L} = \dot{\gamma}\mathbf{e}_1\mathbf{e}_2$ (with \mathbf{e}_1 , \mathbf{e}_2 and \mathbf{e}_3 respectively the flow, gradient and vorticity directions), from which we define the strain-rate tensor $\mathbf{E} = \dot{\gamma}\hat{\mathbf{E}} \equiv (\mathbf{L} + \mathbf{L}^T)/2$. The shear rate $\dot{\gamma}$ is related to the velocity of the top plane relative to the bottom plane $\mathbf{v} = \dot{\gamma}g\mathbf{e}_1$, $g = 1$ mm being the gap width between the two plates.

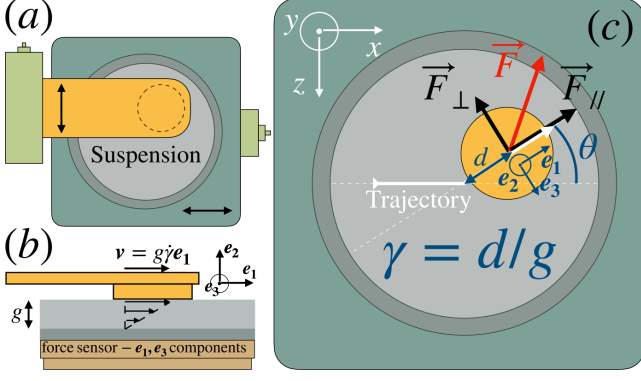


FIG. 1. Sketch of the setup. (a) View along the flow-gradient direction. Two translation stages (light green) independently move an upper plate (orange) and a lower plate (green gray), between which the suspension (light gray) is sheared. (b) Shear plane view. A force sensor measures the tangential stresses. (c) View along the flow-gradient direction of the trajectory (thick white line) of the top plate relative to the bottom plate during a shear rotation by an angle θ . A transient force $\vec{F} = F_{\parallel}e_1 + F_{\perp}e_3$ is recorded after the shear rotation.

A force sensor (AMTI HE6x6-1) measures the tangential force $\vec{F} = \vec{F}_{\parallel} + \vec{F}_{\perp}$ exerted on the lower plate (and thus by the upper plate on the suspension), with \vec{F}_{\parallel} and \vec{F}_{\perp} respectively along e_1 and e_3 (Fig. 1(b)-(c)). We define the shear viscosity $\eta_{12} \equiv \Sigma : e_1 e_2 / \dot{\gamma} = \vec{F}_{\parallel} \cdot e_1 / (S \dot{\gamma})$, with S the area of the upper plate, as well as the ‘‘orthogonal’’ shear viscosity $\eta_{32} \equiv \Sigma : e_3 e_2 / \dot{\gamma} = \vec{F}_{\perp} \cdot e_3 / (S \dot{\gamma})$. Both have opposite θ -parities: η_{12} is even, $\eta_{12}(\gamma, \theta) = \eta_{12}(\gamma, -\theta)$, while η_{32} is odd, $\eta_{32}(\gamma, \theta) = -\eta_{32}(\gamma, -\theta)$ (in particular this enforces that $\eta_{32}(\gamma, 0)$ and $\eta_{32}(\gamma, \pi)$ vanish).

A preshear is first applied over 10 strain units, which is enough to reach steady state, followed by a shear rotation where we rotate the flow direction e_1 and vorticity direction e_3 by an angle $\theta \in [-\pi, \pi]$ around the gradient direction e_2 (thick white line in Fig. 1(c)).

The viscosities $\eta_{12}(\gamma, \theta)$ and $\eta_{32}(\gamma, \theta)$ are recorded via a DAQ (USB-1608FS-PLUS, MCCDAQ) as a function of the subsequent strain $\gamma < 10$. The strain resolution is $\sim 3 \times 10^{-3}$ and the lowest available strain is $\sim 1 \times 10^{-2}$, and θ is sampled every $\pi/18$.

The suspension particles are polystyrene (PS) spheres with a diameter of $40 \mu\text{m}$ (Microbeads TS40). They are dispersed in PEG (Sigma-Aldrich, viscosity $\eta_0 = 38.4 \text{ Pa}\cdot\text{s}$) (resp. silicon oil M1000, Roth, $\eta_0 = 0.98 \text{ Pa}\cdot\text{s}$) for suspensions at $\phi = 0.45$ (resp. $\phi = 0.57$).

Numerics & model We perform the same protocol in DEM simulations of a suspension of $N = 2000$ frictional particles subject to lubrication and contact forces in a tri-periodic configuration, using a method described in [29, 38]. The suspension is bidisperse (with a size ratio 1 : 1.4) and the friction coefficient is $\mu_p = 0.5$.

We also compare our results to the predictions of the GW model, a model capturing the features of shear reversal [35, 36]. The GW model considers the strain evolution of a fabric tensor $\langle nn \rangle$ where \mathbf{n} is the unit separation vector between pairs of particles in a near interaction via contact or lubrication forces

$$\partial_{\gamma} \langle nn \rangle = \hat{\mathbf{L}} \cdot \langle nn \rangle + \langle nn \rangle \cdot \hat{\mathbf{L}}^T - 2\hat{\mathbf{L}} : \langle nnnn \rangle - \beta \left[\hat{\mathbf{E}}_e : \langle nnnn \rangle + \frac{\phi}{15} (2\hat{\mathbf{E}}_c + \text{Tr}(\hat{\mathbf{E}}_c)\delta) \right], \quad (1)$$

with $\hat{\mathbf{E}}_c$ (resp. $\hat{\mathbf{E}}_e$) the compressive (resp. extensive) part of $\hat{\mathbf{E}}$, and β the pair association and dissociation rate, which increases with ϕ . The tensor $\langle nnnn \rangle$ is approximated in terms of $\langle nn \rangle$ with the Hinch & Leal closure [39]. Furthermore, the GW model decomposes the stress $\Sigma = \Sigma^H + \Sigma^C + 2\eta_0 \mathbf{E}$ in contributions from hydrodynamics, Σ^H , and contacts, Σ^C ,

$$\frac{\Sigma^H}{\eta_s \dot{\gamma}} = \alpha \hat{\mathbf{E}} : \langle nnnn \rangle; \quad \frac{\Sigma^C}{\eta_s \dot{\gamma}} = \chi \hat{\mathbf{E}}_c : \langle nnnn \rangle. \quad (2)$$

Here $\alpha = \frac{\alpha_0}{(1-\phi/\phi_{\text{RCP}})^2}$ and $\chi = \frac{\chi_0}{(1-\xi/\xi_J)^2}$, with α_0 and χ_0 free parameters, are such that they diverge respectively at the random close packing volume fraction ϕ_{RCP} and when the ‘jamming coordinate’, which can be interpreted as a proxy for the coordination number, $\xi = -\frac{\langle nn \rangle : \mathbf{E}_c}{|\mathbf{E}_c|}$ reaches the jamming value $\xi_J = \phi_J \frac{(213\beta^2 - 234\beta + 2080)}{15(9\beta^2 + 54\beta + 416)}$ [35, 40], which in steady shear flow occurs at the frictional jamming point, $\phi = \phi_J < \phi_{\text{RCP}}$.

Results In Fig. 2(a), we show the viscosity $\eta_{12}(\gamma, \theta)$ measured in experiments, for a moderately dense suspension at $\phi = 0.45$. It decreases at low strain values, then passes through a minimum before increasing back to its steady-state value. The minimum is located at a strain γ_{min} weakly dependent on θ , from $\gamma_{\text{min}} \approx 0.15$ for $\theta \approx \pi/2$ to $\gamma_{\text{min}} \approx 0.35$ for shear reversal ($\theta = \pi$). As shown in Fig. 2(b), the minimum value $\eta_{12, \text{min}}$ gradually decreases when θ increases, to reach its lowest value for shear reversal. Once normalized by the steady-state value η_{12}^{SS} , $\eta_{12, \text{min}}/\eta_{12}^{\text{SS}}$ for a given θ decreases when ϕ increases, as is already known for shear reversal [23]. Interestingly, for the lowest $\phi = 0.45$, $\eta_{12, \text{min}} \approx \eta_{12}^{\text{SS}}$ for $\theta \lesssim \pi/4$: η_{12} seems oblivious to the shear rotation at small angles, which we could interpret as a non-fragile response. (We will see that this is not quite true when considering η_{32} .)

We compare these data with the DEM ones in a radial representation $\eta_{12}(\gamma, \theta)$ in Fig. 2(d), with experiments in the top half and numerics in the bottom half. The agreement is good, besides simulations predicting a quicker relaxation to steady state than actually observed.

We turn in Fig. 2(e) to η_{32} , again comparing experiments in the top half and numerics in the bottom half. Both datasets are in excellent agreement and reveal

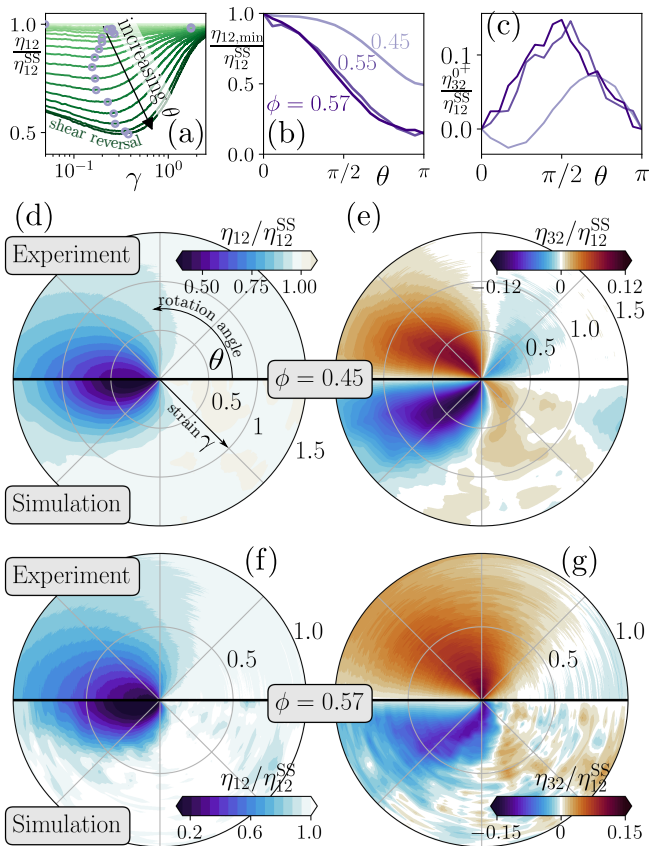


FIG. 2. (a) Shear viscosity η_{12} normalized by the steady-state value η_{12}^{SS} as a function of strain γ in experiments for $\phi = 0.45$, for several values of $\theta \in [0, \pi]$, increasing from light to dark. The minimum values of the viscosity $\eta_{12,\min}/\eta_{12}^{SS}$ for each θ are circled. (b) and (c) $\eta_{12,\min}/\eta_{12}^{SS}$ and (g) orthogonal viscosity just after rotation $\eta_{32}^+/\eta_{12}^{SS}$ as a function of shear rotation angle θ for $\phi = 0.45, 0.55$ and 0.57 . (d) and (e) Polar representation of $\eta_{12}(\gamma, \theta)$ and $\eta_{32}(\gamma, \theta)$, normalized by η_{12}^{SS} , for $\phi = 0.45$, in experiments (top half) and numerical simulations (bottom half). (f) and (g) Same, but for $\phi = 0.57$.

a structure with a mixture of first and second order odd circular harmonics (respectively $\propto \sin\theta$ and $\propto \sin 2\theta$) coming with similar amplitudes. For $0 < \theta \lesssim \pi/2$, we find $\eta_{32} < 0$ for $\gamma \lesssim 1$, i.e. the suspension exerts on the top plate a “restoring” force in the direction of decreasing θ values. In a force control setup where one sets the upper plate force \vec{F}_{\parallel} rather than its displacement, the suspension would thus be stable with respect to shear rotations, by rotating the velocity of the top plate towards lower θ values. By contrast, for $\pi/2 \lesssim \theta < \pi$, we find $\eta_{32} > 0$ for $\gamma \lesssim 2$, which can be interpreted as the suspension tending to rotate the trajectory of the top plate towards larger θ values.

In Fig. 2(f),(g), we show η_{12} and η_{32} for $\phi = 0.57$, close to $\phi_J \approx 0.58$. Both experimental and numerical data show that the relaxation to steady state is quicker than at $\phi = 0.45$, with a smaller $\eta_{12,\min}/\eta_{12}^{SS}$ value [23, 25].

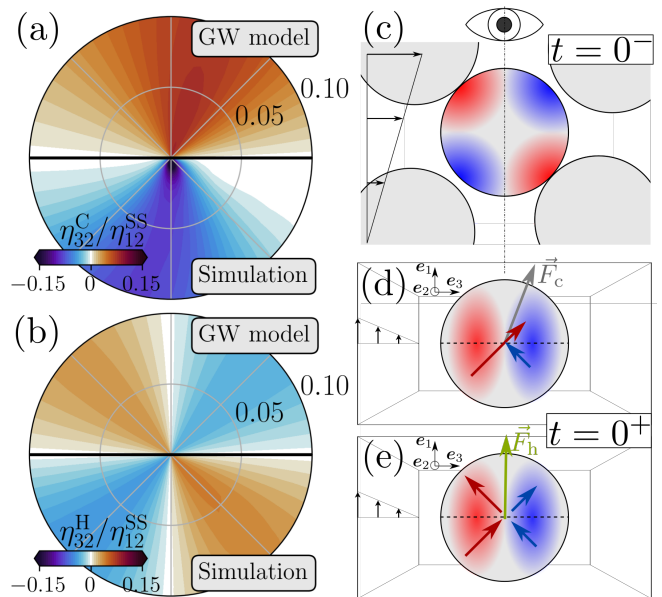


FIG. 3. Contributions to the orthogonal viscosity from contacts (a) and hydrodynamics (b), in the GW model in the top halves and DEM simulations in the bottom halves, for $\phi = 0.45$. Following [36], we chose $\phi_{RCP} = 0.65$, $\phi_J = 0.58$, $\alpha_0 = 2.3$, $\chi_0 = 2.4$, and $\beta = 7$. (c) A particle during initial shear at $t = 0^-$ has more near contacts in compressional quadrants (red) than elongational quadrants (blue). (d)–(e) Looking down from the gradient direction, just after shear rotation by $\theta = \pi/2$ the new compressional and elongational quadrants are respectively below and above the dashed lines. Contact forces come from the new compressional, and are dominated by the more numerous contacts in the old compressional (red arrow), leading to $\eta_{32}^C > 0$ (d). Hydrodynamic forces have symmetric contributions from new compressional and elongational quadrants, leading to $\eta_{32}^H = 0$ (e).

More importantly, the first harmonic of η_{32} dominates. For $0 < \theta < \pi$, we find $\eta_{32} > 0$: the suspension always tend to push the top plate to move towards larger θ values, that is, the response is no longer stabilizing for small shear rotations. In Fig. 2(c), we highlight this qualitative change by showing the θ dependence of the values just after rotation η_{32}^+ .

Our simulations also show that the stress response is closely mimicked by the microstructure response, characterized by the fabric evolution after shear rotation [38]. Notably, however, the fabric evolution does not exhibit any qualitative change upon increase of ϕ that we could correlate to the change of behavior of η_{32} .

To understand the origin of the η_{32} behavior, we interrogate the GW model, performing shear rotations and looking separately at the contact and hydrodynamic contributions to the stress response. As shown in Fig. 3(b), the large second harmonic of η_{32} is due to the hydrodynamic component η_{32}^H , which at $\phi = 0.45$ still accounts for a substantial part of the total stress [30]. In contrast, the contact contribution η_{32}^C has a dominant

first harmonic, with $\eta_{32}^C > 0$ for $0 < \theta < \pi$, as shown in Fig. 3(a). This is confirmed by numerical simulations, which compare well to the predictions of the GW model for both stress components.

The difference between contact and hydrodynamic contributions can be qualitatively understood. In Fig. 3(c), we sketch in the shear plane a particle during preshear. It shows a fore-aft asymmetry: it has more near interactions (lubricated and in contact) in the compressional quadrants (in red) than in the elongational one (in blue). The same particle is seen from the gradient direction \mathbf{e}_2 right after a shear rotation with $\theta = \pi/2$ in Fig. 3(d),(e). After rotation, the fore-aft asymmetry accumulated in preshear is a “left-right” asymmetry, and fore-aft symmetry is temporarily restored. Post-rotation contact stresses (Fig. 3(d)) stem from contacts in the post-rotation compressional quadrant, below the dashed line, and due to the left-right asymmetry, are dominated by contacts that carry over from the pre-rotation in the intersect of pre- and post-rotation compressional quadrants. Contact forces \vec{F}_C in this overlap region (red vector) are such that $\mathbf{e}_3 \cdot \vec{F}_C > 0$, giving a positive contribution to η_{32} . By contrast, in Fig. 3(d), all interactions contribute hydrodynamic forces, and the fore-aft symmetry ensures that the hydrodynamic contribution from the post-rotation elongational and compressional quadrants share the same \mathbf{e}_1 component, but have opposite \mathbf{e}_3 component. This results in a net-zero hydrodynamic contribution to η_{32} .

Whereas this reasoning can be extended to show that $\eta_{32}^C > 0$ for $\theta \in]0, \pi[$, the sign of η_{32}^H for $\theta \neq \pi/2$ depends on aspects of the distribution of near interactions that cannot be deduced from symmetry considerations. The GW model however gives us a quantitative picture alongside a microstructural insight. Calling $\langle \mathbf{nn} \rangle^{\text{ss}}$ the steady-state fabric in pre-shear, we get the following contributions to η_{32} at $\gamma = 0^+$ [38]

$$\begin{aligned} \frac{\eta_{32}^H}{\eta_s} &= \frac{\alpha(\phi)}{14} \sin 2\theta (\langle \mathbf{nn} \rangle_{xx}^{\text{ss}} - \langle \mathbf{nn} \rangle_{zz}^{\text{ss}}) \\ \frac{\eta_{32}^C}{\eta_s} &= \frac{\chi(\xi)}{7} \left[\frac{\sin 2\theta}{4} (\langle \mathbf{nn} \rangle_{xx}^{\text{ss}} - \langle \mathbf{nn} \rangle_{zz}^{\text{ss}}) - \sin \theta \langle \mathbf{nn} \rangle_{xy}^{\text{ss}} \right], \end{aligned} \quad (3)$$

with

$$\xi = \left[\cos^2 \theta \langle \mathbf{nn} \rangle_{xx}^{\text{ss}} + \langle \mathbf{nn} \rangle_{yy}^{\text{ss}} + \sin^2 \theta \langle \mathbf{nn} \rangle_{zz}^{\text{ss}} - 2 \cos \theta \langle \mathbf{nn} \rangle_{xy}^{\text{ss}} \right] / 2.$$

For the contact contribution, the first harmonic dominates for the values of ϕ and β investigated. It is such that $\eta_{32}^C > 0$ for $0 < \theta < \pi$. By contrast, the hydrodynamic contribution only has a second harmonic, and dominates the response at angles close to $\theta = 0$ and $\theta = \pi$. Moreover, its sign is not obvious, as it is set by $\langle \mathbf{nn} \rangle_{xx}^{\text{ss}} - \langle \mathbf{nn} \rangle_{zz}^{\text{ss}}$. With our value of $\beta = 7$, we always find $\langle \mathbf{nn} \rangle_{xx}^{\text{ss}} - \langle \mathbf{nn} \rangle_{zz}^{\text{ss}} < 0$ in the GW model. For small

θ values, it therefore “stabilizes” the microstructure, as $\text{sgn} \eta_{32}^H = -\text{sgn} \theta$, so that it provides a restoring force acting against the rotation of the flow direction. From previous simulations, $\langle \mathbf{nn} \rangle_{xx}^{\text{ss}} - \langle \mathbf{nn} \rangle_{zz}^{\text{ss}}$ is known to be tiny [25]. In our simulations, where we compute $\langle \mathbf{nn} \rangle$ based on particle pairs separated by at most a gap of $\epsilon_c = 0.05$ times the average radius of the pair, we also find $\langle \mathbf{nn} \rangle_{xx}^{\text{ss}} - \langle \mathbf{nn} \rangle_{zz}^{\text{ss}} < 0$, albeit decreasing in amplitude when ϕ increases. Interestingly, the value of $\langle \mathbf{nn} \rangle_{xx}^{\text{ss}} - \langle \mathbf{nn} \rangle_{zz}^{\text{ss}}$ becomes positive for small enough ϵ_c , which highlights how subtle the hydrodynamic stabilization is.

We have shown how to characterize the macro-fragile response of dense suspensions using shear rotations. We performed shear rotations experimentally, numerically, and in a constitutive model, which revealed a rich phenomenology. The shear viscosity exhibits a dip (except at small θ for the smallest ϕ explored here, $\phi = 0.45$) on strain scales of order unity or less, and its amplitude increases upon increase of $|\theta|$ or ϕ increase. Remarkably, whereas in steady state symmetry imposes that η_{32} vanishes, we find that $\eta_{32} \neq 0$ during the transient micro-structure reorganization following a shear rotation, with $|\eta_{32}|$ reaching up to 50% of η_{12} at $\phi = 0.57$, and 10% of η_{12}^{SS} . The qualitative angular structure of $\eta_{32}(\gamma, \theta)$ depends on ϕ , which is explained by the predominance of either hydrodynamic or contact stresses. For $\phi = 0.45$, the second harmonic of $\eta(\gamma, \theta)$ is large as hydrodynamic stresses are significant, while for $\phi = 0.57$ it is small as contact stresses dominate. One consequence is that for small θ , η_{32} produces a force that acts to reduce (stabilize) θ at smaller ϕ while it increases (destabilizes) θ at larger ϕ .

These findings are relevant to virtually all actual flows of suspensions that involve changes in the flow orientation, e.g. extrusions, flows of suspensions in porous materials, and landslides on varying slope directions. The decrease of η_{12} under shear rotations has already been used to suggest energy-saving flow strategies [15, 16], however the behavior of η_{32} has so far been overlooked. Whereas in this work we impose the deformation and measure η_{32} , in many cases one imposes the force or stress. A finite η_{32} may lead to non-trivial trajectories, e.g. during the pulling or the sedimentation of an object in a dense suspension, especially if the suspension is not stable against shear rotations.

We have here focused on shear rotations, which form only a subset of all the flow changes that can happen in a complex geometry. In general one would also need to characterize changes from simple shear to extensional flows, and of course non-uniform flows, which are known to induce migration phenomena [41]. While characterizing all flow histories relevant for applications (or even a carefully selected subset) is a major task, our results show that it would certainly reveal non-trivial yet possibly important stress responses. As the GW model captures the salient features of the stress response under

shear rotation, as well as for non-uniform flows [42], it could also prove an efficient design tool in this endeavour.

Acknowledgements. Work funded in part by the European Research Council under the Horizon 2020 Programme, ERC grant agreement number 740269.

-
- [1] M. M. Denn and J. F. Morris, Annual Review of Chemical and Biomolecular Engineering **5**, 203 (2014).
- [2] C. Ness, R. Seto, and R. Mari, Annual Review of Condensed Matter Physics **13**, 97 (2022).
- [3] G. Ovarlez, F. Bertrand, and S. Rodts, Journal of Rheology (1978-present) **50**, 259 (2006).
- [4] F. Boyer, E. Guazzelli, and O. Pouliquen, Physical Review Letters **107**, 188301 (2011).
- [5] I. E. Zarraga, D. A. Hill, and D. T. L. Jr, Journal of Rheology (1978-present) **44**, 185 (2000).
- [6] S.-C. Dai, E. Bertevras, F. Qi, and R. I. Tanner, Journal of Rheology (1978-present) **57**, 493 (2013).
- [7] T. Dbouk, L. Lobry, and E. Lemaire, Journal of Fluid Mechanics **715**, 239 (2013).
- [8] A. Vázquez-Quesada, R. I. Tanner, and M. Ellero, Physical Review Letters **117**, 108001 (2016).
- [9] L. Lobry, E. Lemaire, F. Blanc, S. Gallier, and F. Peters, Journal of Fluid Mechanics **860**, 682 (2019).
- [10] R. Seto, R. Mari, J. F. Morris, and M. M. Denn, Physical Review Letters **111**, 218301 (2013).
- [11] M. Wyart and M. E. Cates, Physical Review Letters **112**, 098302 (2014).
- [12] G. Ovarlez, Q. Barral, and P. Coussot, Nature materials **9**, 115 (2010).
- [13] Q. Barral, *Superposition d'écoulements orthogonaux dans des fluides complexes: mise en place de l'expérience, application aux suspensions et aux fluides à seuil*, Ph.D. thesis, Université Paris-Est (2011).
- [14] F. Blanc, E. Lemaire, and F. Peters, Journal of Fluid Mechanics **746**, 10.1017/jfm.2014.160 (2014).
- [15] N. Y. C. Lin, C. Ness, M. E. Cates, J. Sun, and I. Cohen, Proceedings of the National Academy of Sciences **113**, 10774 (2016).
- [16] C. Ness, R. Mari, and M. E. Cates, Science Advances **4**, eaar3296 (2018).
- [17] M. Ramaswamy, I. Griniasty, J. P. Sethna, B. Chakraborty, and I. Cohen, Incorporating tunability into a universal scaling framework for shear thickening (2022), arXiv:2205.02184 [cond-mat].
- [18] F. Gadala-Maria and A. Acrivos, Journal of Rheology **24**, 799 (1980), publisher: The Society of Rheology.
- [19] T. Narumi, H. See, Y. Honma, T. Hasegawa, T. Takahashi, and N. Phan-Thien, Journal of Rheology (1978-present) **46**, 295 (2002).
- [20] V. G. Kolli, E. J. Pollauf, and F. Gadala-Maria, Journal of Rheology (1978-present) **46**, 321 (2002).
- [21] F. Blanc, F. Peters, and E. Lemaire, Journal of Rheology (1978-present) **55**, 835 (2011).
- [22] N. Y. C. Lin, B. M. Guy, M. Hermes, C. Ness, J. Sun, W. C. K. Poon, and I. Cohen, Physical Review Letters **115**, 228304 (2015).
- [23] F. Peters, G. Giovanni, S. Gallier, F. Blanc, E. Lemaire, and L. Lobry, Journal of Rheology **60**, 715 (2016).
- [24] C. Ness and J. Sun, Physical Review E **93**, 012604 (2016).
- [25] R. N. Chacko, R. Mari, S. M. Fielding, and M. E. Cates, Journal of Fluid Mechanics **847**, 700 (2018).
- [26] D. Lootens, H. van Damme, Y. Hémar, and P. Hébraud, Physical Review Letters **95**, 268302 (2005).
- [27] F. Blanc, F. Peters, and E. Lemaire, Physical Review Letters **107**, 208302 (2011).
- [28] F. Blanc, E. Lemaire, A. Meunier, and F. Peters, Journal of Rheology (1978-present) **57**, 273 (2013).
- [29] R. Mari, R. Seto, J. F. Morris, and M. M. Denn, Journal of Rheology (1978-present) **58**, 1693 (2014).
- [30] S. Gallier, E. Lemaire, F. Peters, and L. Lobry, Journal of Fluid Mechanics **757**, 514 (2014).
- [31] B. M. Guy, M. Hermes, and W. C. K. Poon, Physical Review Letters **115**, 088304 (2015).
- [32] M. E. Cates, J. P. Wittmer, J.-P. Bouchaud, and P. Claudin, Physical Review Letters **81**, 1841 (1998).
- [33] G. G. Giusteri and R. Seto, Physical Review Letters **127**, 138001 (2021).
- [34] R. Seto, A. Singh, B. Chakraborty, M. M. Denn, and J. F. Morris, Granular Matter **21**, 82 (2019).
- [35] J. J. J. Gillissen and H. J. Wilson, Physical Review E **98**, 033119 (2018).
- [36] J. J. J. Gillissen, C. Ness, J. D. Peterson, H. J. Wilson, and M. E. Cates, Journal of Rheology **64**, 353 (2020), publisher: The Society of Rheology.
- [37] N. Y. C. Lin, J. H. McCoy, X. Cheng, B. Leahy, J. N. Israelachvili, and I. Cohen, Review of Scientific Instruments **85**, 033905 (2014).
- [38] See Supplemental Material at [URL will be inserted by publisher].
- [39] E. J. Hinch and L. G. Leal, J. Fluid Mech. **76**, 187 (1976).
- [40] J. J. J. Gillissen, C. Ness, J. D. Peterson, H. J. Wilson, and M. E. Cates, Physical Review Letters **123**, 214504 (2019).
- [41] É. Guazzelli and O. Pouliquen, Journal of Fluid Mechanics **852**, P1 (2018).
- [42] J. J. J. Gillissen and C. Ness, Physical Review Letters **125**, 184503 (2020).

Supplementary information for “Fragile dense suspensions under shear rotation”

Frédéric Blanc,¹ François Peters,¹ Jurriaan J.J. Gillissen,² Michael E. Cates,³ Sandra Bosio,¹ Camille Benarroche,¹ and Romain Mari⁴

¹*Université Côte d’Azur, CNRS, Institut de Physique de Nice (INPHYNI), France*

²*The Technology Partnership, Science Park, Melbourn, UK.*

³*DAMTP, Centre for Mathematical Sciences, University of Cambridge, Wilberforce Road, Cambridge CB3 0WA, UK*

⁴*Université Grenoble Alpes & CNRS, LIPhy, 38000 Grenoble, France*

(Dated: December 6, 2022)

I. GILLISSEN-WILSON MODEL

A. Model definition

Following Ref. [1], the microstructure $\langle \mathbf{nn} \rangle$ evolution equation reads:

$$\partial_t \langle \mathbf{nn} \rangle = \mathbf{L} \cdot \langle \mathbf{nn} \rangle + \langle \mathbf{nn} \rangle \cdot \mathbf{L}^T - 2\mathbf{L} : \langle \mathbf{nnnn} \rangle - \beta \left[\mathbf{E}_e : \langle \mathbf{nnnn} \rangle + \frac{\phi}{15} (2\mathbf{E}_c + \text{Tr}(\mathbf{E}_c)\boldsymbol{\delta}) \right], \quad (1)$$

where ϕ is the particle volume fraction, \mathbf{L} is the velocity gradient tensor, \mathbf{E} is the deformation rate tensor, \mathbf{E}_c is the compressive part of \mathbf{E} , \mathbf{E}_e is the extensive part of \mathbf{E} and β is the microstructure association rate. The fourth order microstructure tensor $\langle \mathbf{nnnn} \rangle$ is expressed in terms of $\langle \mathbf{nn} \rangle$, using [2]:

$$\begin{aligned} \langle n_i n_j n_k n_l \rangle = & -\frac{1}{35} \langle n_m n_m \rangle (\delta_{ij} \delta_{kl} + \delta_{ik} \delta_{jl} + \delta_{il} \delta_{jk}) \\ & + \frac{1}{7} \left(\delta_{ij} \langle n_k n_l \rangle + \delta_{ik} \langle n_j n_l \rangle + \delta_{il} \langle n_j n_k \rangle + \langle n_i n_j \rangle \delta_{kl} + \langle n_i n_k \rangle \delta_{jl} + \langle n_i n_l \rangle \delta_{jk} \right). \end{aligned} \quad (2)$$

The stress induced by the particles has a hydrodynamic part (first term) and a contact part (second term) and reads:

$$\boldsymbol{\Sigma}' = \eta_0 \left[\frac{\alpha_0 \mathbf{E}}{(1 - \phi/\phi_{\text{RCP}})^2} + \frac{\chi_0 \mathbf{E}_c}{(1 - \xi/\xi_J)^2} \right] : \langle \mathbf{nnnn} \rangle, \quad (3)$$

where η_0 is the solvent viscosity, ϕ_{RCP} is the volume fraction at maximum random packing, α_0 and χ_0 are free parameters, ξ is the ‘jamming coordinate’:

$$\xi = -\frac{\langle \mathbf{nn} \rangle : \mathbf{E}_c}{|\mathbf{E}_c|}, \quad (4)$$

ξ_J is the limiting jamming coordinate, which for frictional systems reads:

$$\xi_J = \phi_J \frac{(213\beta^2 - 234\beta + 2080)}{15(9\beta^2 + 54\beta + 416)}, \quad (5)$$

and ϕ_J is the frictional jamming volume fraction.

B. Shear rotation

We numerically integrate above equations using the Euler forward time integration scheme and the numerical strain step equals 3×10^{-3} . In the numerical experiment we rotate the microstructure in the opposite direction as in the physical experiment, and we keep the shear direction fixed.

Starting from an isotropic microstructure $\langle \mathbf{nn} \rangle = \phi\boldsymbol{\delta}/3$, we apply a xy -shear flow for ten strain units, ensuring that the steady state is reached. Then the microstructure is rotated in the xz -plane over an angle $-\theta$, which is opposite to the rotation angle θ of the flow direction in the physical experiment. Subsequently, a xy -shear flow is applied for two strain units.

Following Ref. [1], we use the following parameter vales: $\phi_{\text{RCP}} = 0.65$, $\phi_J = 0.58$, $\alpha_0 = 2.3$, $\chi_0 = 2.4$, and $\beta = 7$.

C. Post rotation viscosity in the GW model

Here we compute the hydrodynamic and contact contributions to the viscosity η_{12} and η_{32} in simple shear, which are defined as

$$\eta_{12}^{\text{H}} = \Sigma^{\text{H}} : \mathbf{e}_1 \mathbf{e}_2 / \dot{\gamma}, \quad \eta_{32}^{\text{H}} = \Sigma^{\text{H}} : \mathbf{e}_3 \mathbf{e}_2 / \dot{\gamma}, \quad (6)$$

$$\eta_{12}^{\text{C}} = \Sigma^{\text{C}} : \mathbf{e}_1 \mathbf{e}_2 / \dot{\gamma}, \quad \eta_{32}^{\text{C}} = \Sigma^{\text{C}} : \mathbf{e}_3 \mathbf{e}_2 / \dot{\gamma}, \quad (7)$$

with

$$\Sigma^{\text{H}} = \eta_s \frac{\alpha_0}{(1 - \phi/\phi_{\text{RCP}})^2} \mathbf{E} : \langle \mathbf{n} \mathbf{n} \mathbf{n} \mathbf{n} \rangle, \quad (8)$$

$$\Sigma^{\text{C}} = \eta_s \frac{\chi_0}{(1 - \xi/\xi_{\text{J}})^2} \mathbf{E}_c : \langle \mathbf{n} \mathbf{n} \mathbf{n} \mathbf{n} \rangle. \quad (9)$$

We recall that in simple shear, $\mathbf{E} = \dot{\gamma}(\mathbf{e}_1 \mathbf{e}_2 + \mathbf{e}_2 \mathbf{e}_1)/2$, $\mathbf{E}_c = \dot{\gamma}(\mathbf{e}_1 \mathbf{e}_2 + \mathbf{e}_2 \mathbf{e}_1 - \mathbf{e}_1 \mathbf{e}_1 - \mathbf{e}_2 \mathbf{e}_2)/4$. Using Eq. 2, we get the following relation for a symmetric rank-2 tensor \mathbf{A}

$$\begin{aligned} \mathbf{A} : \langle \mathbf{n} \mathbf{n} \mathbf{n} \mathbf{n} \rangle = & -\frac{1}{35} \text{Tr} \langle \mathbf{n} \mathbf{n} \rangle [\text{Tr}(\mathbf{A})\delta + 2\mathbf{A}] \\ & + \frac{1}{7} [\text{Tr}(\mathbf{A})\langle \mathbf{n} \mathbf{n} \rangle + 2\mathbf{A} \cdot \langle \mathbf{n} \mathbf{n} \rangle + 2\langle \mathbf{n} \mathbf{n} \rangle \cdot \mathbf{A} + \mathbf{A} : \langle \mathbf{n} \mathbf{n} \rangle \delta], \end{aligned} \quad (10)$$

so that

$$\eta_{12}^{\text{H}} = \frac{\eta_s}{7} \frac{\alpha_0}{(1 - \phi/\phi_{\text{RCP}})^2} \left[-\frac{1}{5} \text{Tr} \langle \mathbf{n} \mathbf{n} \rangle + \mathbf{e}_1 \cdot \langle \mathbf{n} \mathbf{n} \rangle \cdot \mathbf{e}_1 + \mathbf{e}_2 \cdot \langle \mathbf{n} \mathbf{n} \rangle \cdot \mathbf{e}_2 \right], \quad (11)$$

$$\eta_{12}^{\text{C}} = \frac{\eta_s}{14} \frac{\chi_0}{(1 - \xi/\xi_{\text{J}})^2} \left[-\frac{1}{5} \text{Tr} \langle \mathbf{n} \mathbf{n} \rangle - 3\mathbf{e}_1 \cdot \langle \mathbf{n} \mathbf{n} \rangle \cdot \mathbf{e}_2 + \mathbf{e}_1 \cdot \langle \mathbf{n} \mathbf{n} \rangle \cdot \mathbf{e}_1 + \mathbf{e}_2 \cdot \langle \mathbf{n} \mathbf{n} \rangle \cdot \mathbf{e}_2 \right], \quad (12)$$

$$\eta_{32}^{\text{H}} = \frac{\eta_s}{7} \frac{\alpha_0}{(1 - \phi/\phi_{\text{RCP}})^2} \mathbf{e}_1 \cdot \langle \mathbf{n} \mathbf{n} \rangle \cdot \mathbf{e}_3, \quad (13)$$

$$\eta_{32}^{\text{C}} = \frac{\eta_s}{7} \frac{\chi_0}{(1 - \xi/\xi_{\text{J}})^2} \left[\frac{1}{2} \mathbf{e}_1 \cdot \langle \mathbf{n} \mathbf{n} \rangle \cdot \mathbf{e}_3 - \mathbf{e}_2 \cdot \langle \mathbf{n} \mathbf{n} \rangle \cdot \mathbf{e}_3 \right], \quad (14)$$

with $\xi = [\mathbf{e}_1 \cdot \langle \mathbf{n} \mathbf{n} \rangle \cdot \mathbf{e}_1 + \mathbf{e}_2 \cdot \langle \mathbf{n} \mathbf{n} \rangle \cdot \mathbf{e}_2 - 2\mathbf{e}_1 \cdot \langle \mathbf{n} \mathbf{n} \rangle \cdot \mathbf{e}_2]/2$.

After the shear rotation is applied, we have in Cartesian coordinates $\mathbf{e}_1 = (\cos \theta, 0, -\sin \theta)$, $\mathbf{e}_2 = (0, 1, 0)$, $\mathbf{e}_3 = (\sin \theta, 0, \cos \theta)$. Calling $\langle \mathbf{n} \mathbf{n} \rangle^{\text{ss}}$ the steady-state fabric under xy -shear flow, we get

$$\begin{aligned} \eta_{12}^{\text{H}} = & \frac{\eta_s}{7} \frac{\alpha_0}{(1 - \phi/\phi_{\text{RCP}})^2} \left[-\frac{1}{5} \text{Tr} \langle \mathbf{n} \mathbf{n} \rangle^{\text{ss}} + \langle \mathbf{n} \mathbf{n} \rangle_{yy}^{\text{ss}} + \langle \mathbf{n} \mathbf{n} \rangle_{zz}^{\text{ss}} \right. \\ & \left. + \frac{1}{2} (1 + \cos 2\theta) (\langle \mathbf{n} \mathbf{n} \rangle_{xx}^{\text{ss}} - \langle \mathbf{n} \mathbf{n} \rangle_{zz}^{\text{ss}}) \right], \end{aligned} \quad (15)$$

$$\begin{aligned} \eta_{12}^{\text{C}} = & \frac{\eta_s}{14} \frac{\chi_0}{(1 - \xi/\xi_{\text{J}})^2} \left[-\frac{1}{5} \text{Tr} \langle \mathbf{n} \mathbf{n} \rangle^{\text{ss}} - 3 \cos \theta \langle \mathbf{n} \mathbf{n} \rangle_{xy}^{\text{ss}} \right. \\ & \left. + \frac{1}{2} (1 + \cos 2\theta) (\langle \mathbf{n} \mathbf{n} \rangle_{xx}^{\text{ss}} - \langle \mathbf{n} \mathbf{n} \rangle_{zz}^{\text{ss}}) + \langle \mathbf{n} \mathbf{n} \rangle_{yy}^{\text{ss}} + \langle \mathbf{n} \mathbf{n} \rangle_{zz}^{\text{ss}} \right], \end{aligned} \quad (16)$$

$$\eta_{32}^{\text{H}} = \frac{\eta_s}{14} \frac{\alpha_0}{(1 - \phi/\phi_{\text{RCP}})^2} \sin 2\theta (\langle \mathbf{n} \mathbf{n} \rangle_{xx}^{\text{ss}} - \langle \mathbf{n} \mathbf{n} \rangle_{zz}^{\text{ss}}), \quad (17)$$

$$\eta_{32}^{\text{C}} = \frac{\eta_s}{7} \frac{\chi_0}{(1 - \xi/\xi_{\text{J}})^2} \left[\frac{\sin 2\theta}{4} (\langle \mathbf{n} \mathbf{n} \rangle_{xx}^{\text{ss}} - \langle \mathbf{n} \mathbf{n} \rangle_{zz}^{\text{ss}}) - \sin \theta \langle \mathbf{n} \mathbf{n} \rangle_{xy}^{\text{ss}} \right], \quad (18)$$

with

$$\xi = [\cos^2 \theta \langle \mathbf{n} \mathbf{n} \rangle_{xx}^{\text{ss}} + \langle \mathbf{n} \mathbf{n} \rangle_{yy}^{\text{ss}} + \sin^2 \theta \langle \mathbf{n} \mathbf{n} \rangle_{zz}^{\text{ss}} - 2 \cos \theta \langle \mathbf{n} \mathbf{n} \rangle_{xy}^{\text{ss}}] / 2, \quad (19)$$

where we used that the fabric in steady state under xy -shear flow is such that $\langle \mathbf{n} \mathbf{n} \rangle_{xz}^{\text{ss}} = \langle \mathbf{n} \mathbf{n} \rangle_{yz}^{\text{ss}} = 0$.

For $\beta = 7$, we find that the dipolar component of the contact contribution is dominant over the quadrupolar component. By contrast, the hydrodynamic contribution is quadrupolar, and thus dominates the response at angles close to $\theta = 0$ and $\theta = \pi$.

Moreover, its sign might vary, as it is set by the difference $\langle \mathbf{nn} \rangle_{xx}^{\text{ss}} - \langle \mathbf{nn} \rangle_{zz}^{\text{ss}}$. With the values of β used here, we always find $\langle \mathbf{nn} \rangle_{xx}^{\text{ss}} - \langle \mathbf{nn} \rangle_{zz}^{\text{ss}} < 0$. For small θ values, it therefore “stabilizes” the microstructure, in the sense that $\text{sgn } \eta_{32}^{\text{H}} = -\text{sgn } \theta$, so that it provides a restoring force acting against the rotation of the flow direction.

For a fixed-principal axes material [3] for which we further assume that the fabric shares the principal axes of the strain-rate tensor

$$\langle \mathbf{nn} \rangle = \lambda_c \mathbf{e}_c \mathbf{e}_c + \lambda_e \mathbf{e}_e \mathbf{e}_e + \lambda_v \mathbf{e}_v \mathbf{e}_v \quad (20)$$

with $\mathbf{e}_c = (\mathbf{e}_1 - \mathbf{e}_2)/\sqrt{2}$ the compressional axis, $\mathbf{e}_e = (\mathbf{e}_1 + \mathbf{e}_2)/\sqrt{2}$ the elongational axis, and $\mathbf{e}_v = \mathbf{e}_3$ the vorticity axis, hydrodynamics is stabilizing if $(\lambda_c + \lambda_e)/2 - \lambda_v < 0$.

II. DEM SIMULATIONS

We solve the equations of motions for an assembly of N frictional spheres immersed in a Newtonian fluid with viscosity η_0 , and interacting through hydrodynamic lubrication and contact forces. We use a bidisperse mixture, with spheres of radius either a or $1.4a$. The number ratio of the two populations of spheres is such that each population occupies the same volume.

A. Equations of motion

We consider the case of vanishing Stokes and Reynolds numbers (that is, inertialess fluid and particles), so that the equations of motion can be written as

$$\mathbf{0} = \begin{pmatrix} \mathbf{F}_H \\ \mathbf{T}_H \end{pmatrix} + \begin{pmatrix} \mathbf{F}_C \\ \mathbf{T}_C \end{pmatrix} \quad (21)$$

where $\mathbf{F}_H = \{\mathbf{f}_{H,1}, \dots, \mathbf{f}_{H,N}\}$ and $\mathbf{T}_H = \{\mathbf{t}_{H,1}, \dots, \mathbf{t}_{H,N}\}$ are $3N$ -dimensional hydrodynamic force (resp. hydrodynamic torque) vectors built from the 3-dimensional force (resp. torque) vectors of every particle. Similarly, \mathbf{F}_C and \mathbf{T}_C contain the resultants of contact forces and torques on every particle.

Hydrodynamic forces and torques are coming from Stokes drag and lubrication forces between near particles, and are linearly related to the particles velocities as [4]

$$\begin{pmatrix} \mathbf{F}_H \\ \mathbf{T}_H \end{pmatrix} = -\mathbf{R}_{\text{FU}} \cdot \begin{pmatrix} \mathbf{U}_p - \mathbf{U} \\ \mathbf{\Omega}_p - \mathbf{\Omega} \end{pmatrix} + \mathbf{R}_{\text{FE}} : \mathbf{E}. \quad (22)$$

Here the vectors $\mathbf{U}_p = \{\mathbf{u}_{p,1}, \dots, \mathbf{u}_{p,N}\}$ and $\mathbf{\Omega}_p = \{\boldsymbol{\omega}_{p,1}, \dots, \boldsymbol{\omega}_{p,N}\}$ are respectively the particle translational and angular velocities, which we are solving for. Similarly, $\mathbf{U} = \{\mathbf{u}(\mathbf{r}_1), \dots, \mathbf{u}(\mathbf{r}_N)\}$, $\mathbf{\Omega} = \{\boldsymbol{\omega}(\mathbf{r}_1), \dots, \boldsymbol{\omega}(\mathbf{r}_N)\}$ are the “background” imposed velocities (resp. angular velocities) evaluated at the particles’ centers. Finally, \mathbf{R}_{FU} and \mathbf{R}_{FE} are resp. $6N \times 6N$ and $6N \times N \times 3 \times 3$ resistance tensors, whose elements are given in detail in [5]. They include the leading order of lubrication terms as defined in Jeffrey and Onishi [4] that are diverging when the normalized separation gap $h^{(i,j)} = 2(|\mathbf{r}_j - \mathbf{r}_i| - a_i - a_j)/(a_i + a_j)$ vanishes; they correspond to the “squeeze”, “shear” and “pump” modes of Ball and Melrose [6]. While these terms diverge as either $1/h^{(i,j)}$ or $\log h^{(i,j)}$ for ideally smooth spheres, they are regularized by introducing a roughness length $\delta = 10^{-2}$ such that they scale respectively as $1/(h^{(i,j)} + \delta)$ or $\log(h^{(i,j)} + \delta)$, and they are clipped to their contact value $1/\delta$ or $\log(\delta)$ for $h^{(i,j)} < 0$, that is, when two particles make contact. We consider that two particles i and j interact via lubrication only if their normalized separation gap is such that $0 < h^{(i,j)} < 0.2$.

The contact force on a particle i with radius a_i in contact with particle j can be decomposed in normal and tangential components

$$\mathbf{f}_C^{(i,j)} = \mathbf{f}_{C,\text{nor}}^{(i,j)} + \mathbf{f}_{C,\text{tan}}^{(i,j)}. \quad (23)$$

Contacts fulfill Coulomb’s friction laws $|\mathbf{f}_{C,\text{tan}}^{(i,j)}| \leq \mu_p |\mathbf{f}_{C,\text{nor}}^{(i,j)}|$ with sliding friction coefficient μ_p . The force components $\mathbf{f}_{C,\text{nor}}^{(i,j)}$ and $\mathbf{f}_{C,\text{tan}}^{(i,j)}$ are modeled in a Cundall-Strack fashion [7], with normal and tangential springs

$$\begin{aligned} \mathbf{f}_{C,\text{nor}}^{(i,j)} &= k_n \boldsymbol{\xi}_{C,n}^{(i,j)}, \\ \mathbf{f}_{C,\text{tan}}^{(i,j)} &= k_t \boldsymbol{\xi}_{C,t}^{(i,j)}, \end{aligned} \quad (24)$$

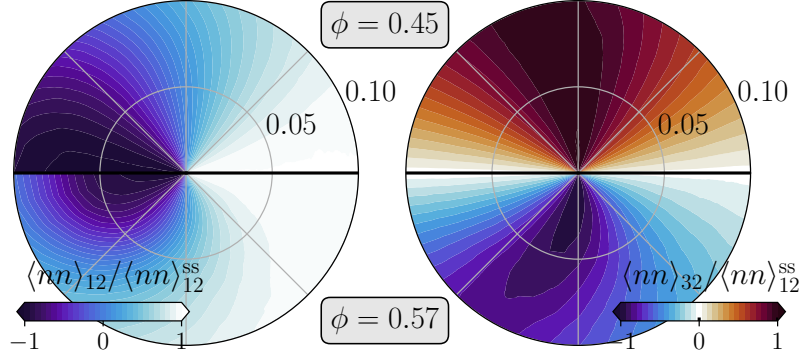


FIG. 1. Evolutions of the $\langle nn \rangle_{12}$ (left) and $\langle nn \rangle_{32}$ components during shear rotation in the DEM simulations, for $\phi = 0.45$ (top halves) and $\phi = 0.57$ (top halves).

where $\xi_{C,n}^{(i,j)} = h^{(i,j)} \mathbf{n}_{ij}$ is the normal spring stretch with $\mathbf{n}_{ij} = (\mathbf{r}_j - \mathbf{r}_i) / |\mathbf{r}_j - \mathbf{r}_i|$ is the unit center-to-center vector, and $\xi_{C,t}^{(i,j)}$ is the tangential spring stretch. Finally, the contact torque on particle i from the contact with particle j is simply obtained as $\mathbf{t}_C^{(i,j)} = a_i \mathbf{n}_{ij} \times \mathbf{f}_C^{(i,j)}$.

B. Stresses

The total stress of the dimer suspension is the sum of the solvent stress and the particle stress

$$\Sigma = 2\eta_0 \mathbf{E} + \Sigma_p, \quad (25)$$

which itself can be decomposed in lubrication stresses and a Kirkwood contribution from contact forces,

$$\Sigma_p = -\mathbf{R}_{SU} \cdot \begin{pmatrix} \mathbf{U}_p - \mathbf{U} \\ \Omega_p - \Omega \end{pmatrix} + \mathbf{R}_{SE} : \mathbf{E} - \frac{1}{2V} \sum_{i < j} [(\mathbf{r}_j - \mathbf{r}_i) \mathbf{f}_C^{(i,j)} + \mathbf{f}_C^{(i,j)} (\mathbf{r}_j - \mathbf{r}_i)], \quad (26)$$

with V the volume of the system.

The particle stress can be further decomposed in hydrodynamic, Σ_p^H , and contact, Σ_p^C components, as [8]

$$\begin{aligned} \Sigma_p^H &= -\mathbf{R}_{SU} \cdot \begin{pmatrix} \delta \mathbf{U}_p^H \\ \delta \Omega_p^H \end{pmatrix} + \mathbf{R}_{SE} : \mathbf{E}, \\ \Sigma_p^C &= -\mathbf{R}_{SU} \cdot \begin{pmatrix} \delta \mathbf{U}_p^C \\ \delta \Omega_p^C \end{pmatrix} - \frac{1}{2V} \sum_{i < j} [(\mathbf{r}_j - \mathbf{r}_i) \mathbf{f}_C^{(i,j)} + \mathbf{f}_C^{(i,j)} (\mathbf{r}_j - \mathbf{r}_i)], \end{aligned} \quad (27)$$

with

$$\begin{aligned} \begin{pmatrix} \delta \mathbf{U}_p^H \\ \delta \Omega_p^H \end{pmatrix} &= \mathbf{R}_{FU}^{-1} \cdot \mathbf{R}_{FE} : \mathbf{E}, \\ \begin{pmatrix} \delta \mathbf{U}_p^C \\ \delta \Omega_p^C \end{pmatrix} &= \mathbf{R}_{FU}^{-1} \cdot \begin{pmatrix} \mathbf{F}_C \\ \mathbf{T}_C \end{pmatrix}. \end{aligned} \quad (28)$$

From these stress components, we get the hydrodynamic contacts components of the viscosity, $\eta_{12}^H = \eta_0 + \Sigma_p^H : \mathbf{e}_1 \mathbf{e}_2 / \dot{\gamma}$, $\eta_{12}^C = \Sigma_p^C : \mathbf{e}_1 \mathbf{e}_2 / \dot{\gamma}$, and of the orthogonal shear viscosity $\eta_{32}^H = \Sigma_p^H : \mathbf{e}_3 \mathbf{e}_2 / \dot{\gamma}$, $\eta_{32}^C = \Sigma_p^C : \mathbf{e}_3 \mathbf{e}_2 / \dot{\gamma}$.

C. Fabric evolution

In this section we briefly describe the observed evolution of the fabric after shear rotation. In Fig. 1, we show the behavior of two components, $\langle nn \rangle_{12} = \langle nn \rangle : \mathbf{e}_1 \mathbf{e}_2$ and $\langle nn \rangle_{32} = \langle nn \rangle : \mathbf{e}_3 \mathbf{e}_2$, in both the moderately concentrated

regime at $\phi = 0.45$ and very concentrated regime $\phi = 0.57$. Besides the decrease of the transient strain scale when increasing ϕ which we also see in the stress response, the two volume fractions show similar behaviors. Upon shear rotation with $|\theta| > \pi/4$, $\langle \mathbf{nn} \rangle_{12} / \langle \mathbf{nn} \rangle_{12}^{\text{ss}}$ decreases, reaches negative values for large $|\theta|$ values and passes through a minimum before relaxing back to its steady-state value. For $|\theta| < \pi/4$, the shear rotation hardly has any measurable effect on $\langle \mathbf{nn} \rangle_{12}$. Just like the orthogonal viscosity, $\langle \mathbf{nn} \rangle_{32} / \langle \mathbf{nn} \rangle_{12}^{\text{ss}}$ shows an antisymmetric behavior with respect to θ , and is positive for $\theta \in [0, \pi]$ and negative for $\theta \in [-\pi, 0]$. It takes values with large amplitudes ≈ 1 before returning to a vanishing steady-state value. In contrast to the viscosity behavior, it does not show a large second order circular harmonic component, even at $\phi = 0.45$.

-
- [1] J. J. J. Gillissen, C. Ness, J. D. Peterson, H. J. Wilson, and M. E. Cates, *Journal of Rheology* **64**, 353 (2020), publisher: The Society of Rheology.
- [2] E. J. Hinch and L. G. Leal, *J. Fluid Mech.* **76**, 187 (1976).
- [3] M. E. Cates, J. P. Wittmer, J.-P. Bouchaud, and P. Claudin, *Physical Review Letters* **81**, 1841 (1998).
- [4] D. J. Jeffrey and Y. Onishi, *J. Fluid Mech.* **139**, 261 (1984).
- [5] R. Mari, R. Seto, J. F. Morris, and M. M. Denn, *Journal of Rheology (1978-present)* **58**, 1693 (2014).
- [6] R. C. Ball and J. R. Melrose, *Physica A* **247**, 444 (1997).
- [7] P. A. Cundall and O. D. L. Strack, *Geotechnique* **29**, 47 (1979).
- [8] J. F. Brady and G. Bossis, *Ann. Rev. Fluid Mech.* **20**, 111 (1988).